Dual Mechanism WS₂-WSe₂ Lateral Monolayer Heterojunction Photodetector and Its Photoresponse Enhancement by Hybridizing with CsPbBr₃ QDs

Shuang Qiao, Jihong Liu, Ruining Wang, Linjuan Guo, Shufang Wang, Anlian Pan,* and Caofeng Pan*

Monolayer 2D lateral heterostructures with high interface qualities and well-defined structures are particularly promising in novel electronic and optoelectronic applications. However, the photoelectric responses are still very low, and the working and modulating mechanisms urgently need exploration. Here, a lateral monolayer heterojunction of WS₂-WSe₂ is successfully prepared with an atomically sharp interface and a band alignment of type-II structure. Intriguingly, this heterojunction photodetector (PD) achieves outstanding characteristics of photocurrent generation in both photovoltaic and photoconductive modes with responsivities (Rs) of 60.2/3.0 A W^{-1}, detectivities (D^*s) of 1.81/0.98 × 10^{12} Jones, and response times of 32.2/28.5 and 39.5/32.1 ms, respectively. Moreover, all-inorganic CsPbBr₃ quantum dots are introduced to substantially promote the photoelectric responses. Because of the favorable band alignment and large absorption of the CsPbBr₃, and efficient carrier transfer, the Rs and D^*s are substantially improved to 1307/141.3 A W^{-1} and 1.16/2.94 × 10^{13} Jones, respectively, with fantastic external quantum efficiencies of 3.59/0.388 × 10^5% and also shortened response times of 12.5/13.2 and 17.4/15.8 ms. In addition, the ambient stability is remarkably enhanced. This study demonstrates that the combination of 2D lateral heterojunction with all-inorganic perovskite may bring up promising opportunities for developing high-performance PDs.

1. Introduction

Benefited from the developments in graphene, two–dimensional (2D) materials have aroused increasing interests recently owing to their remarkable and unique electrical and optical properties, such as high mobility,[1] tunable bandgap,[2] and strong light-matter interactions,[3,4] especially for the monolayer 2D materials.[5–7] Moreover, it has been demonstrated that the atomic heterostructures could show some extraordinary performances and new applications.[8–10] Therefore, different heterojunctions have been prepared. Generally, the heterostructures can be divided into van der Waals (vdWs) heterostructure (vertical) and lateral heterostructure (in-plane) based on the different combining styles.[8,11] The high-quality vdWs heterostructures are constructed by either restacking approach of mechanically exfoliated monolayers or preparing with a multi-step chemical vapor deposition (CVD) technique directly,[9–17] and these heterostructures have been predicted to produce fantastic p-n junctions[15–17] and found to behave numerous novel properties or exotic physics, such as interlayer excitons,[10,13,17] ultrafast carrier transfer and photoresponse,[10] single-electron tunneling[18] and negative differential conductance.[12] However, the interlayer coupling, which has a significant effect on the optical and electrical characteristics of the vdWs heterostructures, could evolve with both the twisted stacking orientations and the qualities of their interfaces,[19–21] and the orientations of the vertical bilayers cannot be exactly controlled. In contrast, lateral heterostructure cannot be created by transfer technique as the allowable accuracy in the in-plane direction of the monolayer is impossible and the chemical atoms in the interface cannot be bonded manually, but only be stitched together by direct epitaxial growth. Since the 2D materials have the similar honeycomb structures, it is conceptually feasible to produce high-quality in-plane heterostructures with the seamless interfaces.[11,22,23] Therefore, the lateral heterojunctions can not only achieve flexible tunability of optical and electrical characteristics via restructuring the monolayer 2D materials but also possess distinct advantages of clean

S. Qiao, C. Pan
Beijing Institute of Nanoenergy and Nanosystems
Chinese Academy of Sciences
Beijing 101400, P. R. China
E-mail: cfpan@binn.cas.cn
S. Qiao, J. Liu, R. Wang, L. Guo, S. Wang
Hebei Key Laboratory of Optic-Electronic Information and Materials, College of Physics Science and Technology
Hebei University
Baoding 071002, P. R. China
A. Pan
Key Laboratory for Micro-Nano Physics and Technology of Hunan Province, State Key Laboratory of Chemo/Biosensing and Chemometrics and College of Materials Science and Engineering
Hunan University
Changsha, Hunan 410082, P. R. China
E-mail: anlian.pan@hnu.edu.cn

**ADVANCED
SCIENCE NEWS**

www.advancedsciencenews.com

**ADVANCED
OPTICAL
MATERIALS**

www.advopticalmat.de

interface,[24] controllable and large-scale production,[25,26] abundant functionality and great promising applications.[23] Till now, some lateral heterostructures have been successfully synthesized and been observed to show excellent rectification behaviors and obvious photocurrent generation properties,[22–26] which are intriguing for developing optoelectronic devices of the monolayer heterostructure. However, from the previous results, high-quality heterojunctions, as well as their applications in photodetectors (PDs), were very rare, and the photoresponse characteristics were still very low.

Fundamentally, the primary reasons of suppressing the performance of the lateral heterojunction PDs can result from the unfavorable band alignment, intrinsic defect, low absorption, and weak stability. It has been explored that interface engineering is a robust solution to overcome these restrictions, and some researchers have achieved huge enhancement of photoresponses in 2D materials by interface modulations of ferroelectric polarization,[27] localized surface plasmon resonance,[28] piezophototronic effect,[29] magnetic-induced-piezopotential,[30] and combining with other low dimensional materials.[31–40] Among them, introducing other outstanding materials, such as perovskite, is thought to be relatively more simple and attractive, as it shows excellent optical absorption, long carrier lifetime, and high carrier mobility,[41] and can be easily prepared on the 2D materials by a low-cost spin-coating technique. However, the previously proposed strategies were mainly studied in a simple single 2D material-based field-effect transistor structure with only one tunable interface. While, different from it, the lateral heterojunction works in diode, and the interface modulations in it are considerably complex as the perovskite can form heterojunctions with both of the 2D materials and may also have an important effect on the interface properties of the lateral heterojunction. Therefore, the related working mechanisms and tuning effects are extremely intriguing and urgently needed to explore.

Herein, a lateral monolayer heterojunction of WS_2-WSe_2 is prepared with a high quality and an atomically sharp interface, and successfully developed as a PD. This PD can work well in both photovoltaic and photoconductive modes, and exhibits extremely outstanding performances with responsivities (Rs) of 60.2 and 3.0 A W^{-1}, detectivities ($D*s$) of 1.81×10^{12} and 9.8×10^{11} Jones, and response times of 32.2/28.5 and 39.5/32.1 ms at forward and reverse biases, respectively. Moreover, considering the intrinsic restriction of the monolayer 2D materials, all-inorganic $CsPbBr_3$ quantum dots (QDs) are introduced to further improve its photoresponses. After preparing a thin layer of $CsPbBr_3$ QDs onto the WS_2-WSe_2 lateral monolayer heterojunction, an innovative perovskite/lateral heterojunction hybrid PD is unprecedentedly acquired. The optimized Rs, $D*s$, and external quantum efficiencies (EQEs), which reach up to 1307/141.3 A W^{-1}, $1.16/2.94 \times 10^{13}$ Jones, and $3.59/0.388 \times 10^5$%, present an enhancement of 21.7/47.1, 6.4/30.1, and 21.7/47.1 times, respectively, and meanwhile, the response times are shortened to 12.5/13.2 and 17.4/15.8 ms. In addition, owning to the protection of the $CsPbBr_3$, the hybrid PD also exhibits a remarkable ambient stability. This work suggests that the combination of 2D lateral heterojunction with all-inorganic perovskite by utilizing their respective advantages and synergistic effect would bring up promising opportunities in high-performance photosensors.

2. Results and Discussion

The optical image of the WS_2-WSe_2 lateral heterostructures is illustrated in **Figure 1**a. Some well-faceted equilateral heterostructure triangles, which are composed of two different parts with obvious color contrast (the core region represents WS_2 with a relatively light color and the shell region represents WSe_2 with relatively dark color), can be observed on the substrate with size even up to about 100 μm, and the surfaces of the heterostructures are very clean. It is supposed that the designed structure of the WS_2-WSe_2 heterostructure is illustrated in Figure 1b, that is, the monolayer WS_2 core is laterally seamed to the WSe_2 shell with a subnanometer sharp heterointerface. Figure 1c gives the atomic force microscope (AFM) result of a typical heterostructure with inset the corresponding line scanning result across both the interface and the edge. A uniform monolayer profile is observed with a height of ≈0.8 nm, indicating the formation of the atomically thin lateral heterojunction. Besides, the atomic resolution elemental and structural measurements have also been previously identified to determine the high crystal quality and atomically sharp interface of the lateral heterojunction by high-resolution scanning transmission electron microscope (HRSTEM), which could be found elsewhere.[42]

To characterize the spatial optical and structural properties, the photoluminescence (PL) and Raman spectra were measured with a confocal excitation laser of 532 nm. The representative PL and Raman results extracted from the three typical positions labeled in Figure 1d are comparatively depicted in Figure 1e,f. The spectra obtained from the shell and core regions of the lateral heterojunction present the special characteristic signals of the monolayer WSe_2 and WS_2, respectively. For the shell WSe_2, the characteristic PL peak is obtained at around 750 nm, which is in accordance with the band edge emission from the monolayer WSe_2 with a band-gap energy of ≈1.65 eV, and a distinct single Raman peak appears at 253.8 cm^{-1}, which arises from the A_{1g} mode of the monolayer WSe_2.[43] While for the core WS_2, the PL peak emerges at around 635 nm, which corresponds to the band edge emission from the monolayer WS_2 with a band-gap energy of ≈1.95 eV, and the remarkable Raman peaks obtained at 170.2, 342.5, and 416.6 cm^{-1} can be attributed to the LA(M), E^1_{2g} and A_{1g} resonance modes of the monolayer WS_2.[44] At the interface, the PL peaks of both the WS_2 and WSe_2 can be observed due to the total effect and co-excitation by the laser. However, there are a small redshift and blueshift of about 5 nm as compared with the core WS_2 and shell WSe_2, respectively, which may result from the abrupt composition change or lattice misfit strain.[42] Similarly, the Raman spectrum also contains the resonance modes of both the WS_2 and WSe_2, confirming the in-plane heterostructure of the WS_2-WSe_2. Moreover, we also evaluated the PL and Raman behaviors with a series of different measurement positions in detail (Figure S1, Supporting Information). With changing the measurement position from the core center to the shell edge, the intensities of both the PL and Raman peaks of the WS_2 decrease and reach zero gradually when approaching the interface, meanwhile, the PL and Raman peaks of the WSe_2 start to appear in overlap and get increasingly strong. Obviously, the spectra of both the WS_2 and WSe_2 still coexist at the interface. However, the shifts of the peak positions are very small, and there are no other peaks of WS_xSe_{2-x} alloys observed
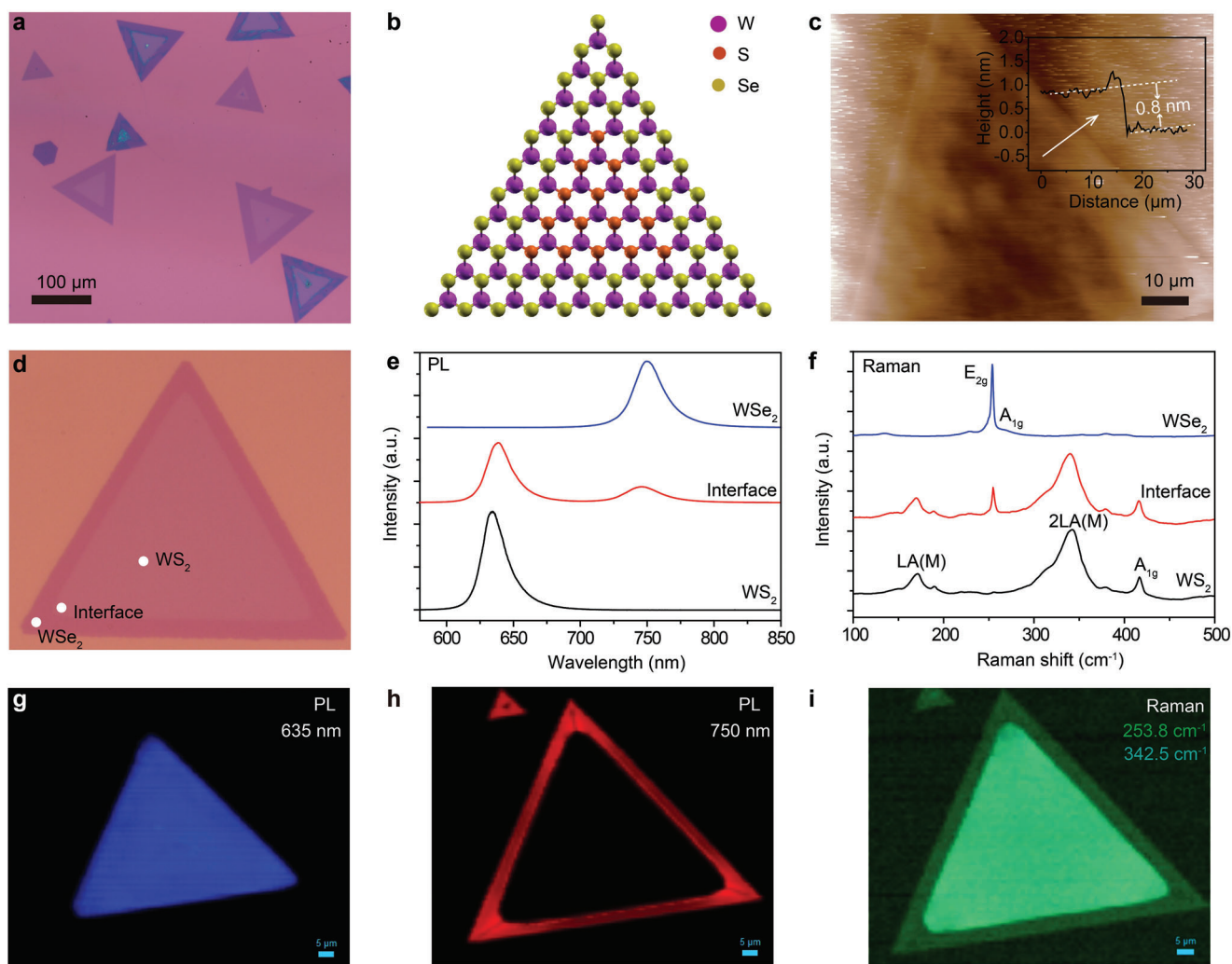
Figure 1. a) Optical image of the as-grown WS_2-WSe_2 lateral heterojunctions. b) Structural model of the monolayer WS_2-WSe_2 lateral heterostructure. c) AFM result of a WS_2-WSe_2 lateral heterojunction, with inset the height profile along the white arrow. d) Optical image of a typical heterojunction labeled three representative positions with the corresponding results of e) PL and f) Raman. PL mapping for the g) WS_2 and h) WSe_2 domains at 635 and 750 nm, respectively. i) Combined Raman mapping for the WS_2-WSe_2 lateral heterojunction at 253.8 and 342.5 cm^{-1}.

in the resolution range, indicating the high interface quality of the lateral heterostructure, which is consistent with the previous HRSTEM results.[42] Besides, the spatially resolved PL and Raman mappings of the WS_2-WSe_2 are further studied by scanning the surface. For the PL mappings, the central wavelengths are set at 635 and 750 nm, respectively, and for the Raman mappings, the central wavenumbers of 253.8 and 342.5 cm^{-1} are selected, respectively. Very homogenous spatial and chemical composition-dependent PL domains can be clearly observed with bright contrast and sharp boundaries: the WS_2 PL domains in the core triangle region as shown in Figure 1g, the WSe_2 PL domains in the peripheral shell region as shown in Figure 1h, and the combined core and shell Raman domains of the WS_2-WSe_2 lateral heterojunction as shown in Figure 1i. Besides, some other typical lateral heterojunctions were also measured with different sizes (Figure S2, Supporting Information), it is demonstrated that both the PL and Raman mappings display very good spatial discrimination for the cores and shells even with a shell width of

only about 4 um, confirming the mature and stable preparation processes. The UV–vis absorption spectrum of the WS_2-WSe_2 is given in Figure S3, Supporting Information. The absorption improves significantly when the wavelength is below ≈760 nm, and two absorption peaks can be observed at ≈640 and ≈750 nm, respectively, which is consistent with the PL results. From the above results, it is indicated that the high-quality lateral monolayer heterojunction of the WS_2-WSe_2 is successfully synthesized.

The lateral heterostructure with high interface quality and well-defined structure is the fundamental premise of creating novel functional optoelectronic devices of the 2D materials. Here, a lateral monolayer heterojunction PD is constructed, with the schematic diagram shown in **Figure 2**a, and the corresponding optical images of the prepared devices can be found in Figure S4, Supporting Information. The WS_2-WSe_2 heterojunctions are wonderfully fabricated into the in-plane heterostructure PDs just as expected. Typically, prior to building this lateral heterojunction as the PD across the in-plane interface, the electrical transport
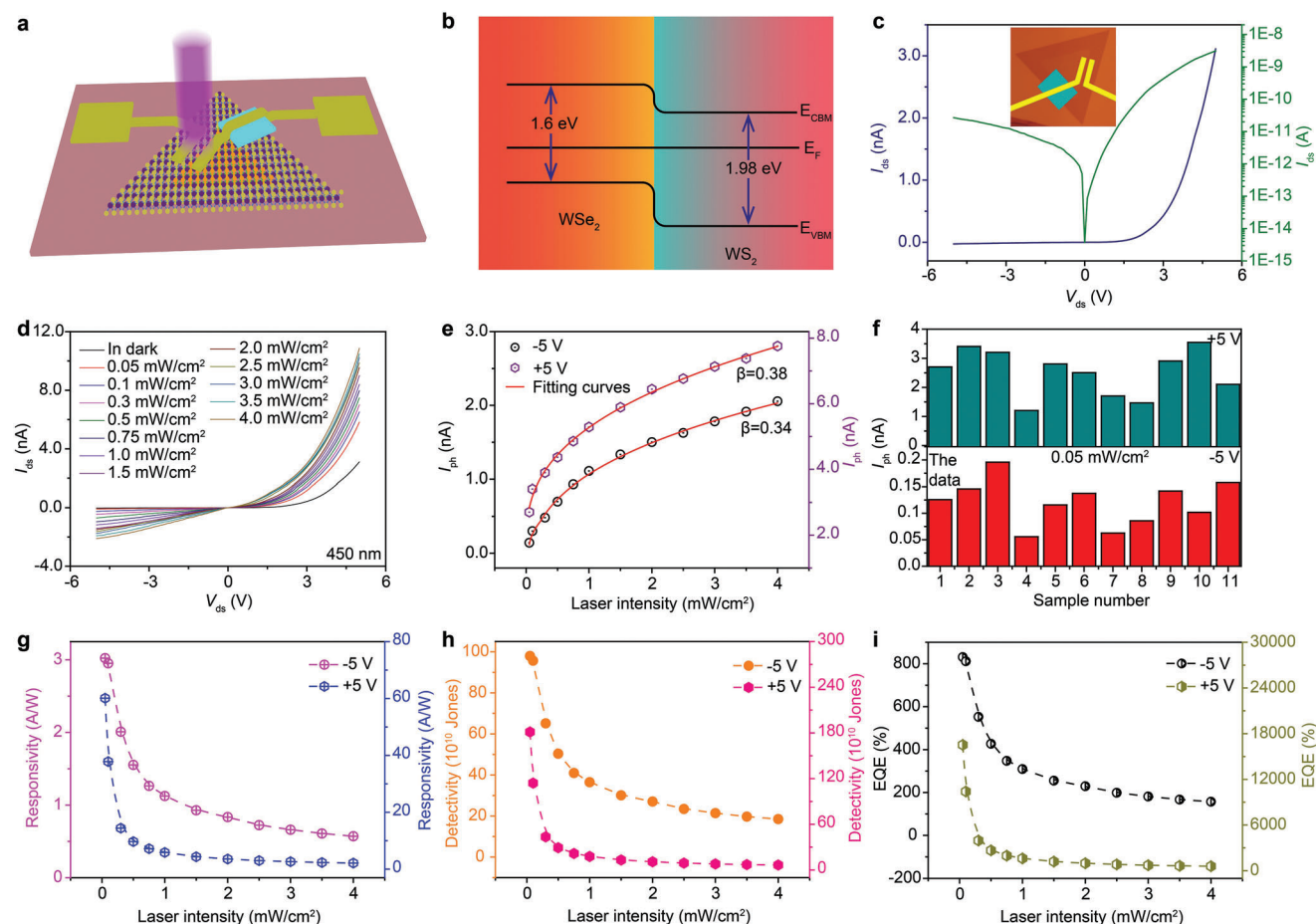
Figure 2. a) Schematic diagram of the WS_2-WSe_2 lateral heterojunction photodetector. b) Equilibrium band alignment of the WS_2-WSe_2 lateral heterojunction in dark. c) I_{ds}–V_{ds} curve measured in dark with inset the optical image of the device. d) I_{ds}–V_{ds} curves measured under different laser intensities of a 450 nm laser. e) The extracted I_{ph} responses at +5 and −5 V. f) Distribution of I_{ph} for different devices under the illumination of 0.05 mW cm^{-2}. The calculated g) Rs, h) D^*s, and i) EQEs at different laser intensities.

characteristics of the core WS_2 and the shell WSe_2 were first evaluated as field-effect transistors, respectively. The drain-source electrodes are Ti/Au layers for the WS_2, and Cr/Pd/Au layers for the WSe_2, and meanwhile the Si substrate is used as a back gate. It is worth mentioning that here the lateral monolayer heterojunction keeps intact, and an insulating layer of Al_2O_3 was precisely patterned and prepared on one side of the shell to avoid it shorting to the core when the contact electrode was crossing through the peripheral WSe_2 to the core WS_2, ruling out the potential chemical modification due to artificial processing, which is quite different from the previous results.[45–47] The typical I_{ds}–V_{BG} curves are shown in Figure S5a,b, from where the clear reverse changing tendencies of the I_{ds} for the WS_2 and WSe_2 can be observed, respectively. The negative dependence of the I_{ds} on the V_{BG} for the WS_2 demonstrates its n-type behavior, and the I_{ds} of the WSe_2 is positively dependent on the V_{BG}, suggesting its p-type characteristic. Moreover, from the I_{ds}–V_{BG} curves, the mobilities were also calculated with the WS_2 ranging from ≈5 to ≈33 cm^2 V^{-1} s^{-1} and the WSe_2 ranging from ≈10 to ≈47 cm^2 V^{-1} s^{-1}, which agree well with the previous findings for the pure WS_2 and WSe_2, respectively.[23,46] In order to further evaluate the electrical properties, the I_{ds}–V_{ds} curves were also studied by applying

different V_{BG}, with the results shown in Figure S5c,d, Supporting Information. The perfect linear relationship of these curves demonstrates the Ohmic contact of these electrodes with either the WS_2 or the WSe_2, so that the contact barriers should have no virtual effect on the intrinsic properties of the lateral heterojunction PD. Because of the specific n-type and p-type features of the WS_2 and WSe_2, a natural p-n lateral monolayer heterojunction should be formed in the WSe_2-WS_2 heterostructure. In addition, the Kelvin force probe microscope measurement has also been utilized to directly quantify the surface potentials in the heterojunction, and a potential difference of ≈113 mV has been observed between the core and the shell regions.[42] Therefore, the WS_2-WSe_2 lateral heterostructure should yield a band alignment of type II heterojunction, where the valence band maximum of the WSe_2 stays in the WS_2, and the conduction band minimum of the WS_2 resides in the WSe_2, as illustrated in Figure 2b.

Then the p-n junction properties of the WS_2-WSe_2 lateral heterostructure were carefully evaluated. For the lateral heterojunction device, the channel width is designed to be 3 μm, and the channel lengths are patterned as 30/20 μm (Figure S4, Supporting Information). Figure 2c gives a typical I_{ds}–V_{ds} curve in dark, which shows a good rectification behavior with the rectification

**ADVANCED
SCIENCE NEWS**

www.advancedsciencenews.com

**ADVANCED
OPTICAL
MATERIALS**

www.advopticalmat.de

ratio reaching up to about 119. The observation of the electrical rectification characteristic directly confirms the emergence of a lateral p-n heterojunction within the WS_2-WSe_2 heterostructure, so that this heterojunction can be built as a monolayer photodiode PD. To evaluate the optoelectronic performances of the device, the I_{ds}−V_{ds} curves were well identified under the illumination of a 450 nm laser, as presented in Figure 2d. A photodiode characteristic is undoubtedly obtained, and the photocurrent improves substantially with laser intensity ranging from 0.05 to 4.0 mW cm^{-2}, implying a high response of this lateral heterojunction as a PD. More importantly, compared with the result in dark, both the forward and backward output currents are largely enhanced when the laser illuminates the device, demonstrating that this lateral heterojunction PD can extraordinarily work well in both photoconductive and photovoltaic modes. Figure 2e gives the laser intensity-dependent photocurrent (I_{ph}) curves at +5 and −5 V, where I_{ph} is extracted by $I_{ph} = I_{light} − I_{dark}$. The I_{ph} increases gradually with increasing the laser intensity, and the relationship could be well fitted by a general equation of $I_{ph} \approx P^\beta$, where P represents the laser intensity. The forward and reverse fitted parameters of β, which are 0.38 and 0.34, respectively, are very close to each other and much lower than the ideal factor of 1, indicating that there are some defects or trap states existing in this heterojunction. Notably, different lateral heterojunction PDs have been measured, and the almost universal photoresponses were obtained with only slight changes in the photocurrents for these devices, as shown in Figure 2f. Then, the key parameters of R and D^* for a PD are estimated based on the equation of $R = I_{ph}/PS$ and $D^* = R/(2eI_{dark}/A)^{0.5}$, respectively, where S represents an effective working area of the device, e represents an elementary electron charge, and I_{dark} represents the output current in dark, respectively. Figure 2g,h gives the calculated results of the R and D^*, respectively. Both the R and D^* go down exponentially with an increase in the laser intensity, which is attributed to the gradually raising probability of carriers' scattering and recombination induced by the trap states as previously reported in other structures.[24,32–34,36–39] In particular, the traping effect gets alleviated in large regimes of the laser intensity, so that the photoresponse tends to be stable finally. Moreover, even though there are some imperfections in the WS_2-WSe_2 lateral monolayer heterojunction, the PD still shows very good performances with Rs as high as 60.2 A W^{-1} at +5 V and 3.0 A W^{-1} at −5 V, and D^* exceeding 1.81×10^{12} Jones at +5 V and 9.8×10^{11} Jones at −5 V, respectively, all of which are not only much superior to the previous results of the similar heterostructure devices, but also comparable to the best results realized in the pristine monolayer 2D materials, as summarized in Table S1, Supporting Information. More importantly, to our knowledge, it is the first time that both the efficient photoconductive and photovoltaic modes are obtained in the lateral monolayer heterostructure, which may be ascribed to the suitable band structure and the highly efficient generation, extraction, and transportation of the carriers in the WS_2-WSe_2 lateral monolayer heterostructure.[23] The EQE of a PD, which is used to evaluate the number of the averaged photo-induced carriers collected per photon to produce the I_{ph}, is another important figure of merit and can be extracted through an equation of EQE $= hcR/e\lambda$ (where h represents the Planck constant, c represents the velocity of light, and λ represents the wavelength of a laser). From Figure 2i, it is clear that the best EQEs of 16527.6% and

831.2% are obtained at +5 and −5 V, respectively, due to the high quality and excellent photoresponse properties of this device. At last, the response speed is also identified by measuring the temporal photocurrent curves under the illumination of 1 mW cm^{-2} at +5 and −5 V. As shown in **Figure 3**a,c, stable and reproducible dynamic photoswitching curves can be observed, that is the photocurrent raises and falls correspondingly under the periodic illuminations of laser on and off. The rise times of 32.3 and 39.5 ms and the fall times of 28.5 and 32.1 ms are deduced by balancing the time intervals of photocurrent from 10% to 90% in forward and reverse conditions, respectively. Notably, the response times are much faster than that of previously observed in the lateral homojunction PDs, and are also on the same order of magnitude as the best results of the CVD or mechanical exfoliated vertical 2D material heterostructure-based PDs (Table S1, Supporting Information).

To evaluate the working mechanisms of the lateral heterojunction PD, the band alignments are given and well analyzed, as illustrated in Figure 3e,f. Due to the type II band alignment, a built-in electric field forms in the interface of the heterojunction, so that when under illumination, the photo-excited electron-hole pairs could be separated and driven into the WS_2 and WSe_2, respectively, resulting in the generation of the photocurrent, which is thought as the photovoltaic mode. When a reverse bias is applied, an energy difference of the Fermi levels can be produced between the two layers, then more electrons are depleted in WS_2 and more holes are depleted in WSe_2, thus an enhancement of the band bending is induced, which is of great benefit to the production of the photocurrent due to the accelerated separation of the carriers. On the contrary, when a bias is forward added, the energy levels of the WS_2 get an increase, whereas the energy levels of the WSe_2 are reduced, giving rise to an ease of their band bending. As the barrier at the interface is largely lowered and even reversed, the electrons could be easily swept from the WS_2 to the WSe_2, and the holes can be easily transported from the WSe_2 to the WS_2, so that an effective tunability of the forward photocurrent is achieved, which is called as the photoconductive mode. With increasing laser intensity gradually, more and more carriers are generated in the lateral monolayer heterojunction, causing an enlargement of the dual output photocurrents.

It is expected that the pursuit of high photoresponse PDs has always been a hot topic worldwide. Although some excellent photoelectric properties have been observed in this WS_2-WSe_2 lateral monolayer heterojunction, they can still be greatly enhanced as the carriers' generation and recombination are restricted by the intrinsic natures, such as low optical absorption and defects. More importantly, the stability of the monolayer 2D materials is very poor, which is extremely not beneficial to the potential applications and urgently needs to be solved. Therefore, the as-prepared all-inorganic $CsPbBr_3$ QDs were uniformly spin-coated onto the surface of the WS_2-WSe_2 lateral heterojunction, with the schematic diagram shown in **Figure 4**a. The transmission electron microscope (TEM) results suggest that the $CsPbBr_3$ QDs are cube-shaped with an average size of about 15 nm, and the crystal quality of the QDs is very high, as shown in Figure S6a, Supporting Information. The structures of the QDs were also characterized by the X-ray diffraction (XRD) measurements (Figure S6b, Supporting Information). Only three diffraction peaks at 15.24°, 21.53°, and 30.69° are clearly observed, which can be
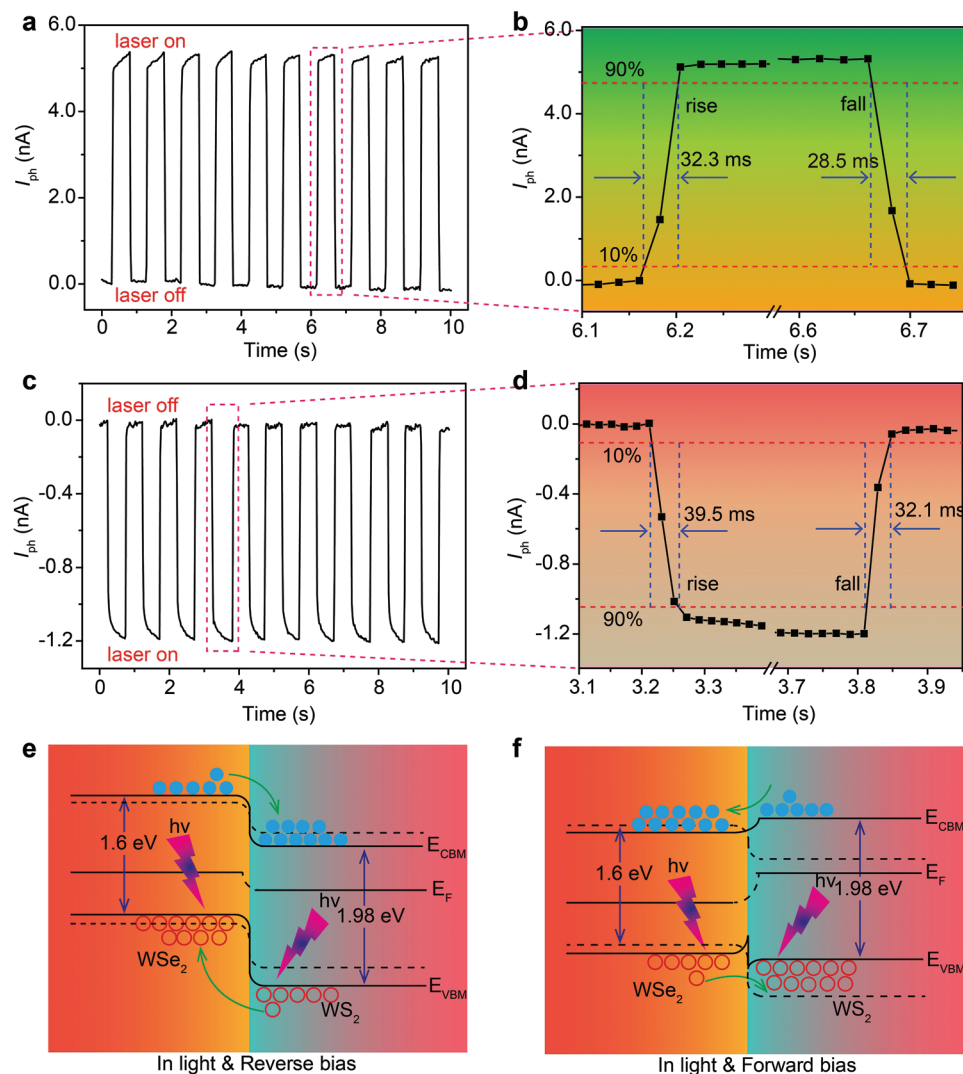
Figure 3. Temporal photocurrent responses at a) +5 V, and c) −5 V under a periodic illumination of 1 mW cm^{-2} with the corresponding enlarged views at laser on and off stages shown in (b) and (d). Schematic diagram of the carrier's generation and separation/transport process in the WS$_2$-WSe$_2$ heterojunction in light at e) reverse bias, and f) forward bias.

assigned as the (100), (110), and (200) crystal indices of the cubic phase CsPbBr$_3$ and the intensities of these peaks even show a moderate enhancement for the sample prepared on the WS$_2$-WSe$_2$, especially the (100) peak, indicating the good crystallinity of the CsPbBr$_3$ QDs in the hybrid heterojunction, which is thought to be beneficial to the reduction of the trap states and thus the improvement of the photoresponse.[34] Besides, in order to characterize the potential phase changing or destroy of the WS$_2$-WSe$_2$ in the hybrid heterojunction, the Raman spectra were well-conducted before and after preparation of the CsPbBr$_3$ QDs to identify the chemical bonding structure, as given in Figure S6c, Supporting Information. Obviously, the Raman peaks of the WS$_2$-WSe$_2$ still keep the same features when measured on the WS$_2$, WSe$_2$, and the interface, respectively. There are no other Raman peaks of the pristine CsPhBr$_3$ or the combining compounds of the CsPbBr$_3$ and the WS$_2$-WSe$_2$, demonstrating that the introduction of the CsPbBr$_3$ QDs has no prominent structural dam-

age in the pristine lateral heterojunction. To qualitatively evaluate the charge transfer property of the hybrid heterojunction, the PL spectra were also identified (Figure S6d, Supporting Information). Here a 325 nm-laser excitation source was employed due to the wider bandgap of the CsPbBr$_3$ at about 2.43 eV.[38,43] Notably, the intrinsic PL peaks of the CsPbBr$_3$ are all observed at about 510 nm when measured at four typical positions, but there exists an immense difference in the intensities of the PL peaks. At the positions with only the CsPbBr$_3$ QDs layer, the relative PL intensity is very strong, in contrast, an outstanding PL peak quenching phenomenon can be observed when the measurement position is moved on the hybrid bilayer of the CsPbBr$_3$ QDs and WS$_2$-WSe$_2$, especially at the interface of the WS$_2$-WSe$_2$ heterojunction, which is consistent with the previously reported results in the single 2D material/perovskite heterostructures.[33,34,36,38,48]

To further determine that the quenching effect is induced by the charge transfer, the time-resolved PL (TRPL) spectra were also
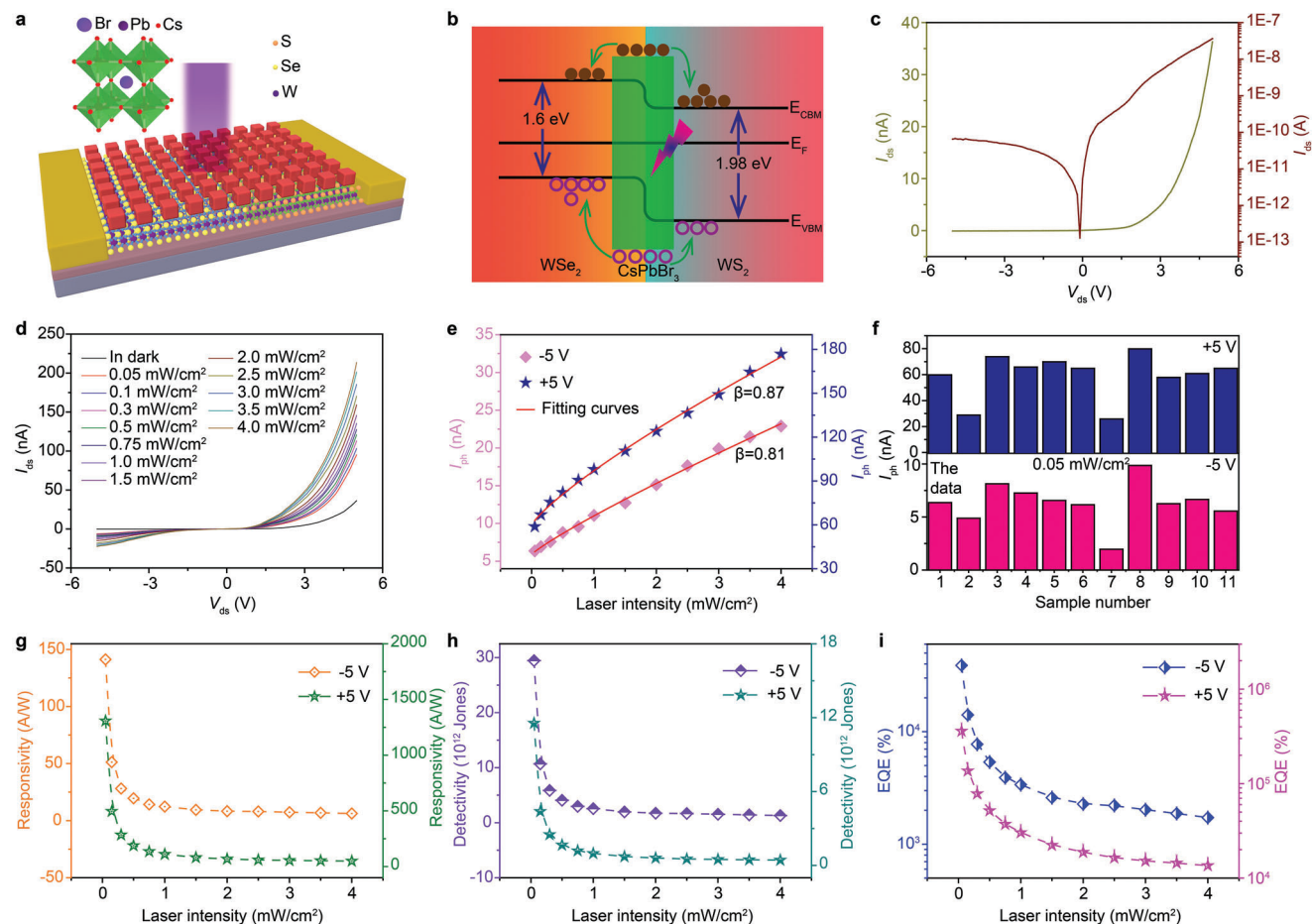
ADVANCED
SCIENCE NEWS

www.advancedsciencenews.com

ADVANCED
OPTICAL
MATERIALS

www.advopticalmat.de

Figure 4. a) Schematic diagram of the hybrid $CsPbBr_3/WS_2$-WSe_2 lateral heterojunction photodetector. b) Schematic diagram of the charge transfer in the hybrid heterostructure under irradiation. c) I_{ds}–V_{ds} curve of the hybrid heterojunction measured in dark. d) I_{ds}–V_{ds} curves of the hybrid heterojunction measured under different laser intensities of a 450 nm laser. e) The extracted I_{ph} responses at +5 and −5 V. f) Distribution of I_{ph} for different hybrid devices under the illumination of 0.05 mW cm^{-2}. The calculated g) Rs, h) D^*s, and i) EQEs at different laser intensities.

carried out, as shown in Figure S6e, Supporting Information. The PL lifetime of the $CsPbBr_3$ QDs is approximately 14.65 ns, and decreases to 7.35 and 6.87 ns when measured on the WS_2 and WSe_2, respectively, and worse still to 2.93 ns at their interface, which directly demonstrates efficient charge transfer from the $CsPbBr_3$ to the WS_2-WSe_2 lateral heterojunction. As shown in Figure S7a, Supporting Information, the conduction band levels of the WS_2, WSe_2, and $CsPbBr_3$ are −4.08, −3.72, and −3.30 eV, and the valence band levels of the WS_2, WSe_2, and $CsPbBr_3$ are −6.03, −5.37, and −5.73 eV, respectively.[38,42] Therefore, when the $CsPbBr_3$ gets contact with either the WS_2 or the WSe_2, the electrons or holes can diffuse from the QDs to the 2D material monolayers, resulting in the aligning of the Fermi levels. The hybrid heterojunctions of the $CsPbBr_3/WS_2$ and $CsPbBr_3/WSe_2$ are expected to produce with the band structures shown in Figure S7b,c, Supporting Information, respectively, and they are also confirmed by the simulation calculations of the band structures (Figure S8, Supporting Information). Importantly, different from the previous results of the phototransistor structures,[33,34,36,37] where the formation of depletion regions induced by the charge transfer can help to suppress the dark currents of the hybrid de-

vices, here a built-in field is originally constructed in the lateral monolayer heterojunction. Therefore the charge transfer could mainly play a vital role in moderately narrowing the depletion region of the lateral heterojunction due to the relative raising and lowering of the band levels for the WS_2 and WSe_2, respectively. Moreover, both of the photo-excited electrons and holes in the conduction band and valence band of the $CsPbBr_3$ could be easily transferred into that of the WS_2 and WSe_2 when under irradiation, respectively, due to the relatively higher conduction band and lower valence band of the $CsPbBr_3$ in the new equilibrium position of the hybrid $CsPbBr_3/WS_2$-WS_2 heterojunction (Figure 4b). It seems that the transferred carriers could aggravate the recombination in the WS_2 and WSe_2, then resulting in the degradation of performance for the hybrid PD. However, these carriers can be quickly separated or swept away on account of the built-in field created in the lateral heterojunction, which may be the fundamental difference from the other 2D material phototransistor structures.[31–40]

Figure 4c illustrates the I_{ds}–V_{ds} curve of the hybrid heterojunction PD in dark. The output current increases clearly as compared with that of the pristine lateral heterojunction, which can

**ADVANCED
SCIENCE NEWS**

www.advancedsciencenews.com

**ADVANCED
OPTICAL
MATERIALS**

www.advopticalmat.de

Table 1. Performance comparisons for hybrid perovskite/2D materials heterostructure-based photodetectors.

Device structure	Laser	Responsivity [A W⁻¹]	Detectivity [Jones]	Response time [ms]	External quantum efficiency (EQE) [%]
Graphene-$CH_3NH_3PbI_3$[33]	520 nm	180	1×10^9	87/540	5×10^4
WS_2-$CH_3NH_3PbI_3$[34]	505 nm	17	2×10^{12}	2.7/7.5	/
WSe_2-$CH_3NH_3PbI_3$[35]	532 nm	110	2.2×10^{11}	143/225	2.5×10^4
MoS_2-$CH_3NH_3PbI_3$[36]	500 nm	1T: 3.3×10^5	1T:7×10^{11}	1T:450/750	1T: 7.7×10^5
		2H:$\approx 10^3$	2H:2.6×10^{11}	2H:25/50	2H: 3.5×10^4
MoS_2-$CsPbI_{3-x}Br_x$[37]	532 nm	7.7×10^4 (@$V_g = 60$ V)	5.6×10^{11}	590/320	$\approx 10^7$
MoS_2-$CsPbBr_3$[38]	442 nm	4.4	2.5×10^{10}	0.72/1.01	302
MoS_2-$CH_3NH_3PbI_3$[39]	520 nm	2.11×10^4 (@$V_g = 20$ V)	1.38×10^{10}	10.7×10^3/6.2×10^3	/
CdS_xSe_{1-x}-$CsPbBr_3$[40]	405 nm	289	1.28×10^{14}	530/620	/
WS_2-$CsPbBr_3$[48]	450 nm	57.2	1.36×10^{14}	2/2	157
MoS_2-$CH_3NH_3Bi_2Br_9$[49]	530 nm	112	3.8×10^{12}	0.3/0.3	/
MoS_2-$(PEA)_2PbI_4$[50]	637 nm	16.8	1.06×10^{13}	6/4	3.3×10^3
MoS_2-$CsPbBr_3$[51]	532 nm	640	3.38×10^{11}	92	1.5×10^3
WS_2-$(C_6H_5C_2H_4NH_3)_2PI_4$[52]	800 nm	7.71×10^{-10}	/	/	/
WS_2-WSe_2/$CsPbBr_3$[this work]	450 nm	1307 (forward)	1.16×10^{13} (forward)	12.5/13.2 (forward)	3.59×10^5 (forward)
		141.3 (reverse)	2.94×10^{13} (reverse)	17.4/15.8 (reverse)	3.88×10^4 (reverse)

be ascribed to an increment of both the concentration of carriers and the equivalent mobility resulting from the band or structure evolution of the lateral heterojunction by introducing $CsPbBr_3$ QDs.[36,38] Moreover, a good rectification relationship can simultaneously be maintained, and the rectification ratio of 519 presents a fantastical enhancement of about 4.6 times. Importantly, this ratio gain has not resulted from the suppression of the reverse current but is mainly due to the great boosting of the forward output. It is worth mentioning that during the experiment, the $CsPbBr_3$ QDs were prepared on the WS_2-WSe_2 heterojunction with different spin speeds ranging from 1000 to 4000 Hz, and the hybrid device prepared at 3000 Hz showed the best performances, as shown in Figure S9, Supporting Information. Therefore, here the hybrid devices were all prepared at this condition. The I_{ds}−V_{ds} results of the hybrid device under a 450 nm laser irradiation are plotted in Figure 4d. The photoresponse of this hybrid PD still improves significantly with the laser intensity increasing from 0.05 to 4.0 mW cm⁻². Figure 4e shows the calculated photocurrents. By fitting the curves with $I_{ph} \approx P^\beta$, the β parameters of 0.81 and 0.87 are obtained at +5 and −5 V, respectively. The obvious advance in β suggests that the $CsPbBr_3$ QDs are also beneficial to diminishing the trap states in the lateral heterojunction. Moreover, the photocurrent improvements are obtained in all the devices of the different hybrid heterojunctions, especially with the comparable amplitude, demonstrating the intrinsic enhancing properties by introducing the $CsPbBr_3$ QDs (Figure 4f). Figure 4g,h displays the extracted Rs and $D*$s, respectively. Owing to the strong light absorption, efficient carrier transfer, and trap states passivation effect of the $CsPbBr_3$ QDs, the optoelectronic performances of the hybrid PD enhances substantially with photoresponsivity as high as 1307 A W⁻¹ at +5 V and 141.3 A W⁻¹ at −5 V, which is about 21.7 times and 47.1 times as compared with that of the pristine lateral monolayer heterojunction, and detectivity reaching up to 1.16×10^{13} Jones at +5 V and 2.94×10^{13} Jones at −5 V, which gets an increment of about 6.4 and 30.1 times, respectively. Besides, this

hybrid PD also yields extremely high EQEs of 3.59×10^5% and 3.88×10^4% (Figure 4i). In order to clarify the excellent performances of the $CsPbBr_3$/WS_2-WSe_2 hybrid PD, the comparison with other devices of the perovskite-modulated 2D material structures is summarized in **Table 1**. The R and $D*$ are one to three and two to four orders of magnitude larger than the previous results without any back gate voltage, respectively. In the case of high photoresponses, a reliable and fast response speed is urgently needed for developing as a high-performance PD. Then the temporal photocurrent responses of the hybrid heterojunction were determined, as presented in **Figure 5**a,c. The photocurrent still shows a clearly periodic on/off photoswitching behavior, and keeps the stable maximum and minimum over multiple cycles, implying the robust and reproducible photoresponse of this hybrid PD. The deduced response times are given in Figure 5b,d. At forward bias, the rise and fall times descended to 12.5 and 13.2 ms, respectively, while at reverse bias, the rise and fall times were calculated to be 17.4 and 15.8 ms, respectively. The obvious improvements in the response speeds as compared with the pristine PD should be attributed to two reasons: one is the trap passivation induced by the $CsPbBr_3$ so that the transport of charge carriers is facilitated, and the other is ultrafast charge transfer from the $CsPbBr_3$ to the WS_2-WSe_2 as the photocurrent of the PD based on the hybrid $CsPbBr_3$/WS_2-WSe_2 heterojunction should be mainly dominated by the transfer of photo-generated carriers in the $CsPbBr_3$,[48] the ultrafast transfer speed, as well as the efficient carrier separation and transport of the lateral heterojunction, ensures these faster response times.

Then, to explain the working mechanism of the hybrid lateral heterojunction, the band alignment is also well analyzed, as presented in Figure 5e,f. In the equilibrium state, a barrier can not only be produced at the interface of the WS_2-WSe_2 but also be built at the interfaces of the $CsPbBr_3$/WS_2 and $CsPbBr_3$/WSe_2 (Figure S6b,c, Supporting Information). Similar to the pristine lateral heterojunction, the band levels of the WS_2 and WSe_2 shift downward and upward, respectively when a bias is reversely

**ADVANCED
SCIENCE NEWS**

www.advancedsciencenews.com

**ADVANCED
OPTICAL
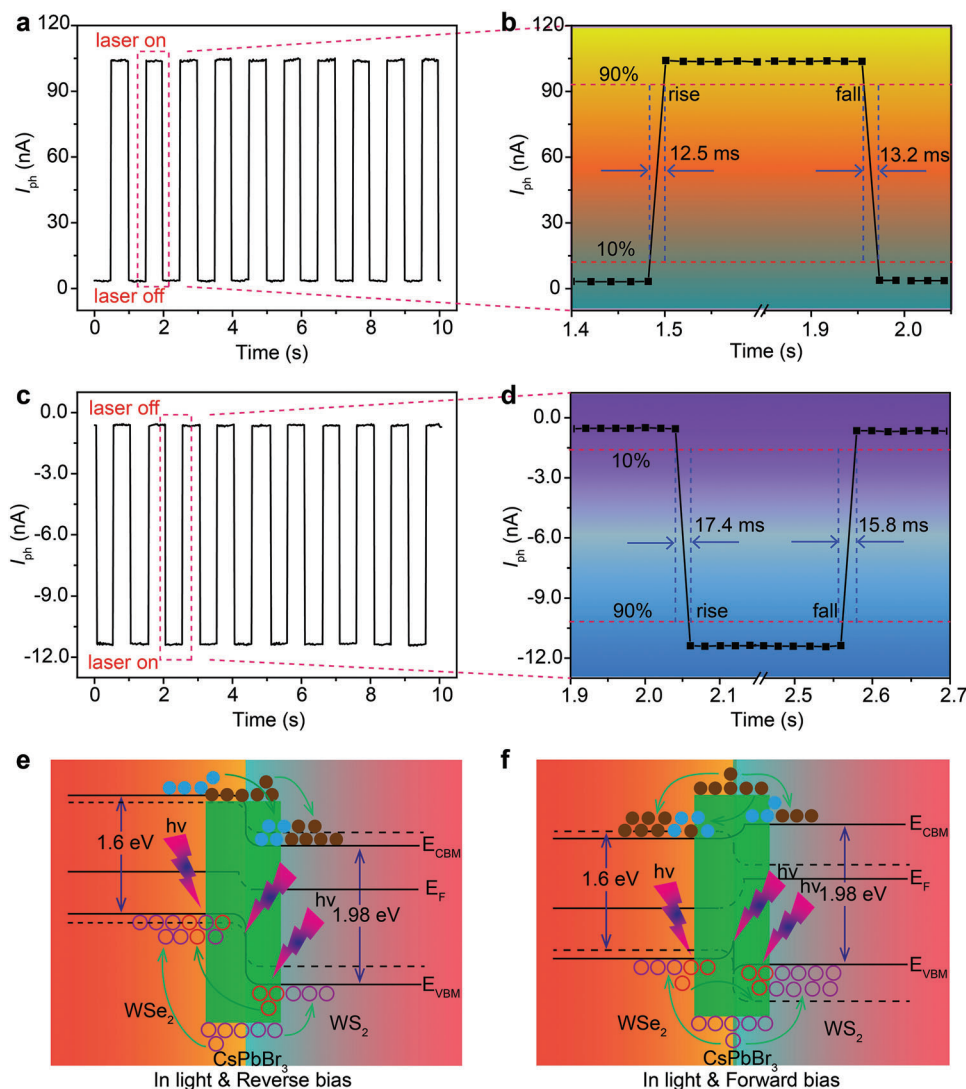MATERIALS**

www.advopticalmat.de

Figure 5. Temporal photocurrent responses of the hybrid heterojunction at a) +5 V, and c) −5 V under a periodic illumination of 1 mW cm^{-2} with the corresponding enlarged views at laser on and off stages shown in (b) and (d). Schematic diagram of the carrier's generation, transfer, and separation/transport process in the hybrid CsPbBr$_3$/WS$_2$-WSe$_2$ lateral heterojunction in light at e) reverse bias, and f) forward bias.

applied, resulting in an increase of the potential difference. However, the band levels of the CsPbBr$_3$ are approximately supposed to keep constant, so that the relative band levels between the CsPbBr$_3$ and the WS$_2$-WSe$_2$ should be realigned, as illustrated in Figure 5e. While under irradiation of a laser, the photo-generated carriers in the CsPbBr$_3$ would quickly transfer into the lateral heterojunction. In particular, the electrons and holes that transferred into the WS$_2$ and WSe$_2$, respectively, could directly contribute to the output of photocurrent. Still, the holes entering into the WS$_2$ should be separated by the interface field at first and then transport into the WSe$_2$ just as the photo-generated carriers in the pristine lateral heterojunction, which is also beneficial to the enhancement of the photocurrent. When applying a forward bias, owing to the injection of non-equilibrium minority carriers, the Fermi levels of the WS$_2$ and WSe$_2$, and also the conduction and valence levels, are relatively raised and lowered, respectively, giving rise to a large reduction of the barrier. At this

moment, the band levels of the WS$_2$-WSe$_2$ are demonstrated to reside in the CsPbBr$_3$, as given in Figure 5f. Therefore, both the electrons and holes generated in the CsPbBr$_3$ can transfer into the WS$_2$ and WSe$_2$ due to its higher conduction level and lower valence level, and then directly produce the photocurrent or be swept away and transmitted subsequently to gain the photocurrent.

Besides, the photoresponse properties were also studied under the illumination of different incident lasers with a wavelength range of 405–980 nm to better understand the interactions of the CsPbBr$_3$ and WS$_2$-WSe$_2$ in the hybrid lateral heterojunction. The typical I_{ds}−V_{ds} results at an illumination intensity of 1 mW cm^{-2} are plotted in **Figure 6**a. The photoresponses are strongly dependent on the laser wavelength as the photocurrents are very high when it is shorter than 532 nm, then decrease quickly at the illumination wavelengths larger than 532 nm (Figure 6b). This can be well understood as the incident photon energies of the 405
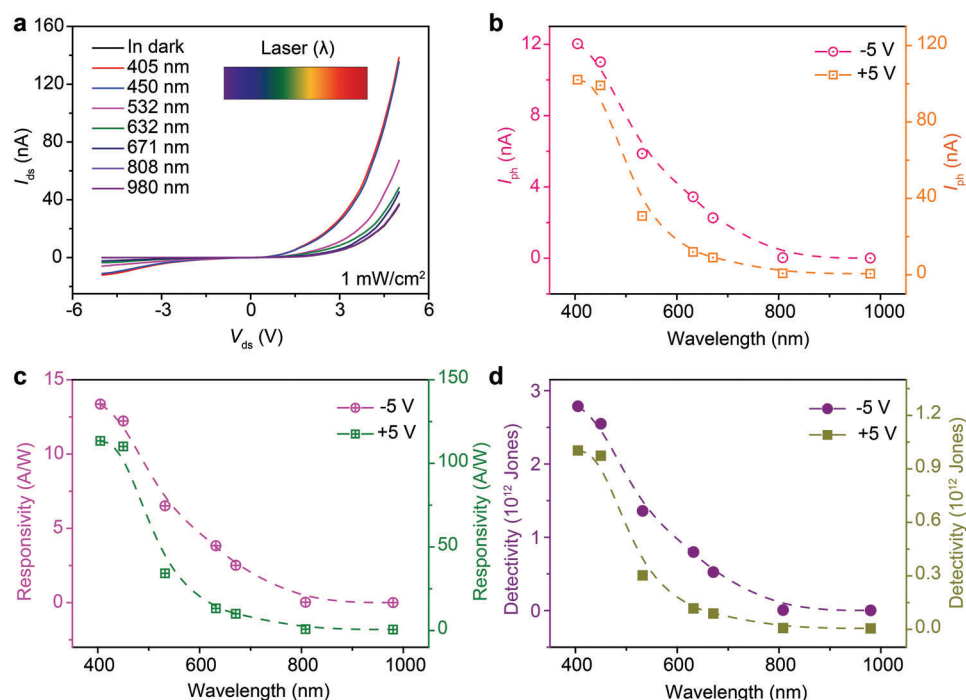
Figure 6. a) I_{ds}–V_{ds} curves of the hybrid heterojunction measured under different irradiation wavelengths at a fixed laser intensity of 1 mW cm^{-2}. b) The extracted wavelength-dependent I_{ph} responses at +5 and −5 V. The calculated c) R and d) D^* as a function of laser wavelength.

and 450 nm are larger than the bandgap energy of the CsPbBr$_3$ and can be completely absorbed, resulting in a large increment in the density of photogenerated carriers, and thus arousing the improvement of the photocurrents. With the wavelength ranging from 532 to 671 nm, the absorption, which is mainly dominated by the WS$_2$-WSe$_2$, is very small, so that the photoresponse declines sharply. When the wavelength exceeds 671 nm, the generation is almost impossible in both the CsPbBr$_3$ and the WS$_2$-WSe$_2$, that may be why no observable photocurrent is obtained (the I_{ds} is nearly equivalent with that in dark). Figure 6c,d gives the calculated laser wavelength-dependent R and D^* at +5 and −5 V. Similarly, the changing tendencies of the R and D^* can also be ascribed to the different excitation efficiency of carriers in the hybrid heterojunction. Moreover, even though the Rs and D^*s at the 632 and 671 nm are much smaller than those at the 405 or 450 nm, they are still substantially enhanced as compared with that of the pristine PD, which should result from the advance of both the concentration of carriers and the equivalent mobility induced by the highly efficient charge transfer and trap passivation effect of the CsPbBr$_3$.[36,38] Moreover, in order to testify that the photoresponse improvement in the hybrid PD is derived from the synergistic effect of the CsPbBr$_3$ and WS$_2$-WSe$_2$, the CsPbBr$_3$ phototransistor was also prepared and investigated under the illumination of a 450 nm-laser with laser intensity over a range of 0.05–4.0 mW cm^{-2}, as shown in Figure S10a, Supporting Information. There is a clear photoresponse when under irradiation, and the photocurrent increases gradually with laser intensity (Figure S10b, Supporting Information). Notably, the photocurrent is a little larger than that of the WS$_2$-WSe$_2$ lateral heterojunction PD (especially in larger laser intensities), but it is much lower than that of the hybrid device. Figure S10c,d,

Supporting Information illustrates the laser intensity-dependent R and D^*, respectively. The best R of the CsPbBr$_3$ phototransistor is 36.6 A W^{-1}, and the D^* can reach up to 7.8 × 10^{11} Jones. Notably, both of the key factors are comparable to or even some larger than the previously reported results,[53,54] but are 35.7 and 37.7 times lower as compared with that of the hybrid CsPbBr$_3$ QDs and WS$_2$-WSe$_2$ lateral monolayer heterojunction PD.

At last, the ambient stabilities of the devices were investigated before and after preparing the CsPbBr$_3$ QDs. The PDs were preserved under an ambient condition (≈35% RH and ≈24 °C) without any encapsulation over a period of 1–14 days. **Figure 7a** gives the time-dependent photocurrent responses of the pristine WS$_2$-WSe$_2$ PD. It is clear that the photocurrent starts to decrease after about 48 h, and is reduced by half after 1 week. Worse still, 2 weeks later, there is no output current gotten due to the complete deterioration of the device. In contrast, the hybrid device shows excellent stability as there is no degradation of the photocurrent during the 14 days (Figure 7b). The stability improvement of the hybrid PD can be mainly ascribed to two reasons: one is the relatively stable characteristics of the all-inorganic CsPbBr$_3$ QDs as it can not only keep itself high stability in the air but also protect the WS$_2$-WSe$_2$ from exposing to the atmosphere; the other is the different structure from the previous results where the perovskite is the main working layer (light absorption and carrier transport), so that the slight deterioration of the CsPbBr$_3$ can make an important effect on the performances. While, in the CsPbBr$_3$/WS$_2$-WSe$_2$ hybrid PD, the main working layer is the WS$_2$-WSe$_2$ heterojunction, and the CsPbBr$_3$ is only the top modifying layer, so that the PD can still work well even the CsPbBr$_3$ is slightly deteriorated. The high optoelectronic performances, together with the outstanding stability, highlight that the hybrid structures of
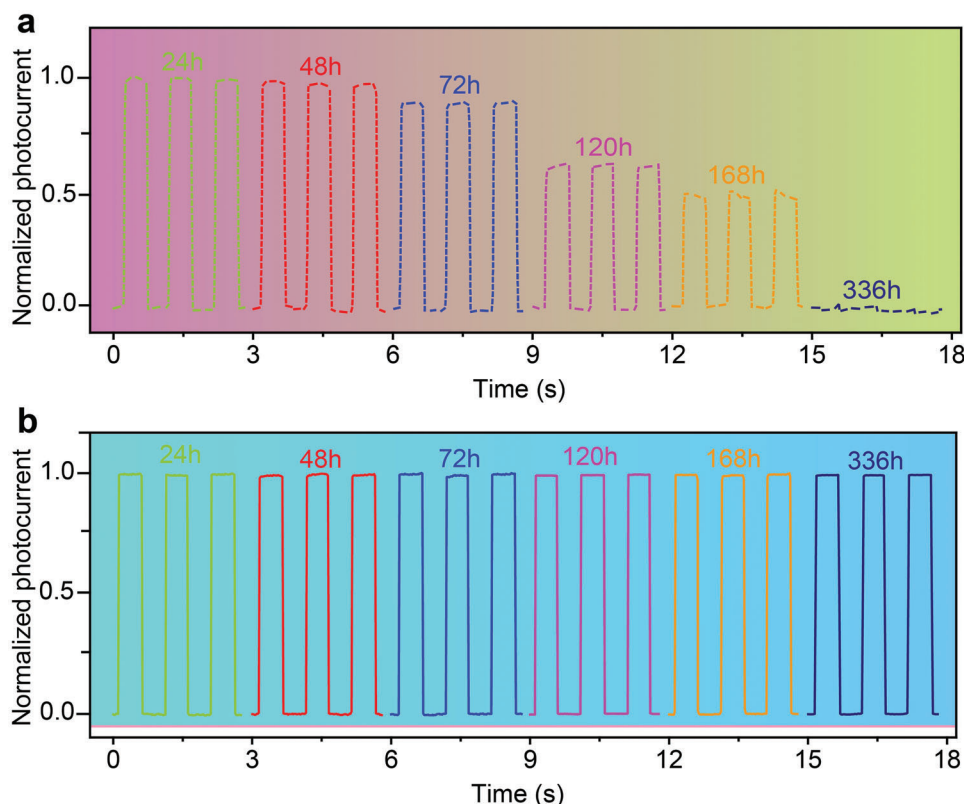
**ADVANCED
SCIENCE NEWS**

www.advancedsciencenews.com

**ADVANCED
OPTICAL
MATERIALS**

www.advopticalmat.de

Figure 7. Temporal photocurrent response curves of the a) pristine WS$_2$-WSe$_2$ lateral heterojunction and b) hybrid CsPbBr$_3$/WS$_2$-WSe$_2$ lateral heterojunction device after preserving in air for different days.

all-inorganic perovskite/lateral monolayer heterojunction may show great potential for achieving future high-performance photodetection.

3. Conclusion

In summary, a monolayer photodiode PD based on the lateral heterojunction of WS$_2$-WSe$_2$ is prepared and well-identified. This PD exhibits excellent optoelectronic performances in both photovoltaic and photoconductive modes with responsivities (Rs) of 60.2 and 3.0 A W^{-1}, detectivities (D*s) of 1.81×10^{12} and 9.8×10^{11} Jones, and response times of 32.2/28.5 and 39.5/32.1 ms, respectively, which may be due to the high crystal quality and the suitable type-II band alignment of the lateral heterostructure. Moreover, in order to further improve its photoresponses and stability, the combination with the all-inorganic CsPbBr$_3$ quantum dots (QDs) is systemically studied. Owning to the favorable band structure, large absorption, and efficient carrier transfer, the optimized Rs (1307/141.3 A W^{-1}), D*s ($1.16/2.94 \times 10^{13}$ Jones), and external quantum efficiencies (EQEs) ($3.59/0.388 \times 10^5$%) of the hybrid PD are enhanced by 21.7/47.1 times, 6.4/30.1 times, and 21.7/47.1 times, respectively, and meanwhile, the response times are also shortened to 12.5/13.2 and 17.4/15.8 ms. In addition, an outstanding ambient stability is obtained in the hybrid PD due to the protection of the all-inorganic perovskite layer. This work provides a significant insight into not only enhancing the photoresponses but also the stability of 2D lateral monolayer

heterojunction-based optoelectronic devices by combining with the all-inorganic perovskite materials.

4. Experimental Section

Preparation of WS$_2$-WSe$_2$:   The monolayer WS$_2$-WSe$_2$ lateral heterojunction was synthesized by physical vapor deposition technique. Briefly, pure WS$_2$ and WSe$_2$ powders were loaded in the left and right zones of an equipment of furnace, respectively, and a SiO$_2$/Si wafer was placed at the center of the two heating zones. At first, Ar was passed through with a constant flow rate of ≈60 SCCM to clean the quartz tube for 20 min; then, the left zone was quickly heated to 1050 °C and the right zone was heated to 1000 °C; after that, Ar was introduced to carry the WS$_2$ vapor source (from left to right) to the target wafer for 5 min; subsequently, the Ar was reversely flowed for 5 min, enabling the further lateral growth of the WSe$_2$ monolayer; at last, the furnace was naturally cooled to ambient temperature. Details of the preparation can be found elsewhere.[42]

Device Fabrication: There were mainly three steps for preparing the lateral heterojunction PD. Step 1: a polymethyl methacrylate (PMMA) layer was first spin-coated on the substrate and baked at 150 °C for 5 min; then the electrodes on the WSe$_2$ layer were designed by the electron beam lithography (EBL); subsequently, Cr/Pd/Au (10/10/50 nm) metal layers were prepared by electron beam evaporation; finally the sample was washed in the acetone to clean the surface. Step 2: the PMMA layer was spin-coated again; then the insulating layers across through the edge WSe$_2$ layer were patterned by EBL, and a Al$_2$O$_3$ insulating layer with thickness of 50 nm was finally prepared by the atomic layer deposition. Step 3: a PMMA layer was third spin-coated; then the electrodes on the WS$_2$ layer were constructed by EBL, and Ti/Au (10/50 nm) layers were grown, followed by the cleaning process with the acetone; at last the devices were

**ADVANCED
SCIENCE NEWS**

www.advancedsciencenews.com

**ADVANCED
OPTICAL
MATERIALS**

www.advopticalmat.de

successfully prepared with a channel width of 3 μm and channel lengths of 20 or 30 μm. For the perovskite/WS$_2$-WSe$_2$ hybrid device, CsPbBr$_3$ QDs solution (2.0 mg mL^{-1}) was directly spin-coated onto the WS$_2$-WSe$_2$ heterojunction with spin frequency ranging from 1000 to 4000 Hz, and then the device was heated at 50 °C for 10 min to remove the organic solvent.

Characterizations and Measurements: The morphologies of the WS$_2$-WSe$_2$ lateral heterojunctions were measured by an optical microscope and AFM (Bruker Multimode 8). PL and Raman spectrums were identified by a commercial Raman equipment (LabRAM HR Evolution) with an excitation laser of 325 or 532 nm. The TRPL was performed by a home-built confocal fluorescence lifetime system. The structure of CsPbBr$_3$ quantum dots was measured by the TEM and XRD. The electrical characteristics of the devices were conducted with a semiconductor parameter analyzer (Keithley 4200) performing on a vacuum probe station (10^{-6} torr, Lake Shore) at ambient temperature. Seven lasers (405, 450, 532, 632, 671, 808, and 980 nm) were totally used as the incident light sources, and the time responses were identified by a DS345 and SR570 (Stanford) system with a periodical laser illumination controlled by a mechanical chopper.

Supporting Information

Supporting Information is available from the Wiley Online Library or from the author.

Conflict of Interest

The authors declare no conflict of interest.

Data Availability Statement

The data that support the findings of this study are available from the corresponding author upon reasonable request.

[1] B. Radisavljevic, A. Radenovic, J. Brivio, V. Giacometti, A. Kis, *Nat. Nanotechnol.* **2011**, *6*, 147.

[2] M. Chhowalla, H. S. Shin, G. Eda, L. J. Li, K. P. Loh, H. Zhang, *Nat. Chem.* **2013**, *5*, 263.

[3] L. Britnell, R. M. Ribeiro, A. Eckmann, R. Jalil, B. D. Belle, A. Mishchenko, Y. J. Kim, R. V. Gorbachev, T. Georgiou, S. V. Morozov, A. N. Grigorenko, A. K. Geim, C. Casiraghi, A. H. Castro Neto, K. S. Novoselov, *Science* **2013**, *340*, 1311.

[4] W. J. Yu, Y. Liu, H. L. Zhou, A. X. Yin, Z. Li, Y. Huang, X. F. Duan, *Nat. Nanotechnol.* **2013**, *8*, 952.

[5] O. L. Sanchez, D. Lembke, M. Kayci, A. Radenovic, A. Kis, *Nat. Nanotechnol.* **2013**, *8*, 497.

[6] B. W. H. Baugher, H. O. H. Churchill, Y. Yang, P. Jarillo-Herrero, *Nat. Nanotechnol.* **2014**, *9*, 262.

[7] Y. H. Chang, W. J. Zhang, Y. H. Zhu, Y. Han, J. Pu, J. K. Chang, W. T. Hsu, J. K. Huang, C. L. Hsu, M. H. Chiu, T. Takenobu, H. N. Li, C. Wu, W. H. Chang, A. T. S. Wee, L. J. Li, *ACS Nano* **2014**, *8*, 8582.

[8] A. K. Geim, I. V. Grigorieva, *Nature* **2013**, *499*, 419.

[9] Y. J. Gong, J. H. Lin, X. L. Wang, G. Shi, S. D. Lei, Z. Lin, X. L. Zou, G. L. Ye, R. Vajtai, B. I. Yakobson, H. Terrones, M. Terrones, B. K. Tay, J. Lou, S. T. Pantelides, Z. Liu, W. Zhou, P. M. Ajayan, *Nat. Mater.* **2014**, *13*, 1135.

[10] X. P. Hong, J. Kim, S. F. Shi, Y. Zhang, C. H. Jin, S. Tongay, J. Q. Wu, Y. F. Zhang, F. Wang, *Nat. Nanotechnol.* **2014**, *9*, 682.

[11] M. P. Levendorf, C. J. Kim, L. Brown, P. Y. Huang, R. W. Havener, D. A. Muller, J. Park, *Nature* **2012**, *488*, 627.

[12] M. H. Chiu, C. D. Zhang, H. W. Shiu, C. P. Chuu, C. H. Chen, C. Y. S. Chang, C. H. Chen, M. Y. Chou, C. K. Shih, L. J. Li, *Nat. Commun.* **2015**, *6*, 7666.

[13] P. Rivera, J. R. Schaibley, A. M. Jones, J. S. Ross, S. F. Wu, G. Aivazian, P. Klement, K. Seyler, G. Clark, N. J. Ghimire, J. Q. Yan, D. G. Mandrus, W. Yao, X. D. Xu, *Nat. Commun.* **2015**, *6*, 6242.

[14] Y. M. He, A. Sobhani, S. D. Lei, Z. H. Zhang, Y. J. Gong, Z. H. Jin, W. Zhou, Y. C. Yang, Y. Zhang, X. F. Wang, B. Yakobson, R. Vajtai, N. J. Halas, B. Li, E. Q. Xie, P. Ajayan, *Adv. Mater.* **2016**, *28*, 5126.

[15] T. F. Yang, B. Y. Zheng, Z. Wang, T. Xu, C. Pan, J. Zou, X. H. Zhang, Z. Y. Qi, H. J. Liu, Y. X. Feng, W. D. Hu, F. Miao, L. T. Sun, X. F. Duan, A. L. Pan, *Nat. Commun.* **2017**, *8*, 1906.

[16] M. M. Furchi, A. Pospischil, F. Libisch, J. Burgdorfer, T. Mueller, *Nano Lett.* **2014**, *14*, 4785.

[17] P. Rivera, J. Ross, J. Schaibley, E. W. Lee, H. Y. Yu, T. Taniguchi, K. Watanabe, J. Q. Yan, D. Mandrus, D. Cobden, W. Yao, X. D. Xu, *Nano Lett.* **2017**, *17*, 638.

[18] G. Kim, S. S. Kim, J. Jeon, S. I. Yoon, S. Hong, Y. J. Cho, A. Misra, S. Ozdemir, J. Yin, D. Ghazaryan, M. Holwill, A. Mishchenko, D. V. Andreeva, Y. J. Kim, H. Y. Jeong, A. R. Jang, H. J. Chung, A. K. Geim, K. S. Novoselov, B. H. Sohn, H. S. Shin, *Nat. Commun.* **2019**, *10*, 230.

[19] K. H. Liu, L. M. Zhang, T. Cao, C. H. Jin, D. Qiu, Q. Zhou, A. Zettl, P. D. Yang, S. G. Louie, F. Wang, *Nat. Commun.* **2014**, *5*, 4966.

[20] J. Zhang, J. H. Wang, P. Chen, Y. Sun, S. Wu, Z. Y. Jia, X. B. Lu, H. Yu, W. Chen, J. Q. Zhu, G. B. Xie, R. Yang, D. X. Shi, X. L. Xu, J. Y. Xiang, K. H. Liu, G. Y. Zhang, *Adv. Mater.* **2016**, *28*, 1950.

[21] J. Zhang, H. Hong, C. Lian, W. Ma, X. Z. Xu, X. Zhou, H. X. Fu, K. H. Liu, S. Meng, *Adv. Sci.* **2017**, *4*, 1700086.

[22] C. M. Huang, S. F. Wu, A. M. Sanchez, J. J. P. Peters, R. Beanland, J. S. Ross, P. Rivera, W. Yao, D. H. Cobden, X. D. Xu, *Nat. Mater.* **2014**, *13*, 1096.

[23] X. D. Duan, C. Wang, J. C. Shaw, R. Cheng, Y. Chen, H. L. Li, X. P. Wu, Y. Tang, Q. L. Zhang, A. L. Pan, J. H. Jiang, R. Q. Yu, Y. Huang, X. F. Duan, *Nat. Nanotechnol.* **2014**, *9*, 1024.

[24] M. Y. Li, Y. M. Shi, C. C. Cheng, L. S. Lu, Y. C. Lin, H. L. Tang, M. L. Tsai, C. W. Chu, K. H. Wei, J. H. He, W. H. Chang, K. Suenaga, L. J. Li, *Science* **2015**, *349*, 524.

[25] Z. W. Zhang, P. Chen, X. D. Duan, K. T. Zang, J. Luo, X. F. Duan, *Science* **2017**, *357*, 788.

[26] P. K. Sahoo, S. Memaran, Y. Xin, L. Balicas, H. R. Gutierrez, *Nature* **2018**, *553*, 63.

**ADVANCED
SCIENCE NEWS**

www.advancedsciencenews.com

**ADVANCED
OPTICAL
MATERIALS**

www.advopticalmat.de

[27] X. D. Wang, P. Wang, J. L. Wang, W. D. Hu, X. H. Zhou, N. Guo, H. Huang, S. Sun, H. Shen, T. Lin, M. H. Tang, L. Liao, A. Q. Jiang, J. L. Sun, X. J. Meng, X. S. Chen, W. Lu, J. H. Chu, *Adv. Mater.* **2015**, *27*, 6575.

[28] Y. Liu, R. Cheng, L. Liao, H. L. Zhou, J. W. Bai, G. Liu, L. X. Liu, Y. Huang, X. F. Duan, *Nat. Commun.* **2011**, *2*, 579.

[29] X. Q. Liu, X. N. Yang, G. Y. Gao, Z. Y. Yang, H. T. Liu, Q. Li, Z. Lou, G. Z. Shen, L. Liao, C. F. Pan, Z. L. Wang, *ACS Nano* **2016**, *10*, 7451.

[30] Y. D. Liu, J. M. Guo, A. F. Yu, Y. Zhang, J. Z. Kou, K. Zhang, R. M. Wen, Y. Zhang, J. Y. Zhai, Z. L. Wang, *Adv. Mater.* **2018**, *30*, 1704524.

[31] G. Konstantatos, M. Badioli, L. Gaudreau, J. Osmond, M. Bernechea, F. P. G. Arquer, F. Gatti, F. H. L. Koppens, *Nat. Nanotechnol.* **2012**, *7*, 363.

[32] D. Kufer, I. Nikitskiy, T. Lasanta, G. Navickaite, F. H. L. Koppens, G. Konstantatos, *Adv. Mater.* **2015**, *27*, 176.

[33] Y. B. Lee, J. Kwon, E. Hwang, C. H. Ra, W. J. Yoo, J. H. Ahn, J. H. Park, J. H. Cho, *Adv. Mater.* **2015**, *27*, 41.

[34] C. Ma, Y. M. Shi, W. J. Hu, M. H. Chiu, Z. X. Liu, A. Bera, F. Li, H. Wang, L. J. Li, T. Wu, *Adv. Mater.* **2016**, *28*, 3683.

[35] J. P. Lu, A. Carvalho, H. W. Liu, S. X. Lim, A. H. C. Neto, C. H. Sow, *Angew. Chem.* **2016**, *128*, 12124.

[36] Y. Wang, R. Fullon, M. Acerce, C. E. Petoukhoff, J. Yang, C. Chen, S. Du, S. K. Lai, S. P. Lau, D. Voiry, D. O'Carroll, G. Gupta, A. D. Mohite, S. D. Zhang, H. Zhou, M. Chhowalla, *Adv. Mater.* **2017**, *29*, 1603995.

[37] H. L. Wu, H. N. Si, Z. H. Zhang, Z. Kang, P. W. Wu, L. X. Zhou, S. C. Zhang, Z. Zhang, Q. L. Liao, Y. Zhang, *Adv. Sci.* **2018**, *5*, 1801219.

[38] X. F. Song, X. H. Liu, D. J. Yu, C. X. Huo, J. P. Ji, X. M. Li, S. L. Zhang, Y. S. Zou, G. Y. Zhu, Y. J. Wang, M. Z. Wu, A. Xie, H. B. Zeng, *ACS Appl. Mater. Interfaces* **2018**, *10*, 2801.

[39] D. H. Kang, S. R. Pae, J. Shim, G. Yoo, J. Jeon, J. W. Leem, J. S. Yu, S. Lee, B. Shin, J. H. Park, *Adv. Mater.* **2016**, *28*, 7799.

[40] M. F. Peng, Y. L. Ma, L. Zhang, S. Cong, X. K. Hong, Y. H. Gu, Y. W. Kuang, Y. S. Liu, Z. Wen, X. H. Sun, *Adv. Funct. Mater.* **2021**, *31*, 2105051.

[41] G. R. Yettapu, D. Talukdar, S. Sarkar, A. Swarnkar, A. Nag, P. Ghosh, P. Mandal, *Nano Lett.* **2016**, *16*, 4838.

[42] B. Y. Zheng, C. Ma, D. Li, J. Y. Lan, Z. Zhang, X. X. Sun, W. H. Zheng, T. F. Yang, C. G. Zhu, G. Ouyang, G. Z. Xu, X. L. Zhu, X. Wang, A. L. Pan, *J. Am. Chem. Soc.* **2018**, *140*, 11193.

[43] P. Tonndorf, R. Schmidt, P. Bottger, X. Zhang, J. Borner, A. Liebig, M. Albrecht, C. Kloc, O. Gordan, D. R. T. Zahn, S. M. Vasconcellos, R. Bratschitsch, *Opt. Express* **2013**, *21*, 4908.

[44] N. Peimyoo, J. Z. Shang, C. X. Cong, X. N. Shen, X. Y. Wu, E. K. L. Yeow, T. Yu, *ACS Nano* **2013**, *7*, 10985.

[45] K. Chen, X. Wan, J. X. Wen, W. G. Xie, Z. W. Kang, X. L. Zeng, H. J. Chen, J. B. Xu, *ACS Nano* **2015**, *9*, 9868.

[46] J. Y. Chen, W. Zhou, W. Tang, B. B. Tian, X. X. Zhao, H. Xu, Y. P. Liu, D. C. Geng, S. J. R. Tan, W. Fu, K. P. Loh, *Chem. Mater.* **2016**, *28*, 7194.

[47] W. H. Wu, Q. Zhang, X. Zhou, L. Li, J. W. Su, F. K. Wang, T. Y. Zhai, *Nano Energy* **2018**, *51*, 45.

[48] Q. Xu, Z. Yang, D. F. Peng, J. G. Xi, P. Lin, Y. Cheng, K. H. Liu, C. F. Pan, *Nano Energy* **2019**, *65*, 104001.

[49] J. He, Y. Yang, Y. He, C. Ge, Y. Zhao, L. Gao, J. Tang, *ACS Photonics* **2018**, *5*, 1877.

[50] H. L. Wang, X. D. Wang, Y. Chen, S. K. Zhang, W. Jiang, X. Zhang, J. J. Qin, J. Wang, X. G. Li, Y. Y. Pan, F. C. Liu, Z. J. Shi, H. J. Zhang, L. Q. Tu, H. L. Wang, H. B. Long, D. P. Li, T. Lin, J. L. Wang, Y. Q. Zhan, H. Shen, X. J. Meng, J. H. Chu, *Adv. Opt. Mater.* **2020**, *8*, 1901402.

[51] L. Zhang, S. Shen, M. Li, L. Li, J. Zhang, L. Fan, F. Cheng, C. Li, M. Zhu, Z. Kang, J. Su, T. Zhai, Y. Gao, *Adv. Opt. Mater.* **2019**, *7*, 1801744.

[52] Q. Wang, A. T. S. Wee, *ACS Nano* **2021**, *15*, 10437.

[53] Y. Li, Z. F. Shi, S. Li, L. Z. Lei, H. F. Ji, D. Wu, T. T. Xu, Y. T. Tian, X. J. Li, *J. Mater. Chem. C* **2017**, *5*, 8355.

[54] G. Q. Tong, H. Li, D. T. Li, Z. F. Zhu, E. Z. Xu, G. P. Li, L. W. Yu, J. Xu, Y. Jiang, *Small* **2018**, *14*, 1702523.